



Theory of Kerr instability amplification

M. NESRALLAH,^{1,*} G. VAMPA,¹ G. BART,¹ P. B. CORKUM,^{1,2} C. R. McDONALD,¹ AND T. BRABEC¹

¹Department of Physics, University of Ottawa, Ottawa, Ontario K1N 6N5, Canada

²National Research Council of Canada, Ottawa, Ontario K1A 0R6, Canada

*Corresponding author: mnesr024@uottawa.ca

Received 20 September 2017; revised 5 February 2018; accepted 10 February 2018 (Doc. ID 307348); published 7 March 2018

Evolution of lasers in Kerr nonlinear materials is inextricably linked with unstable behavior. Current research has investigated the growth of optical Kerr instability out of noise, which results in phenomena such as conical emission and filamentation in bulk materials, and modulation instability in optical fibers. Here, we suggest that seeding Kerr instability in dielectrics can be used for wideband optical amplification ranging from the second harmonic of the pump laser to the mid-infrared. Our theoretical feasibility analysis focuses on the infrared. We find that one- to two-cycle pulse amplification by 3–4 orders of magnitude in the wavelength range of 1–14 μm is feasible with currently available laser sources. Final output energies in the range of a few tens of μJ are achievable corresponding to about 0.25% of the pump energy. Such intense ultrashort mid-infrared radiation sources will substantially impact research in nonlinear spectroscopy, strong-field physics, attosecond science, and ultrafast laser electron accelerators.

© 2018 Optical Society of America under the terms of the OSA Open Access Publishing Agreement

OCIS codes: (190.0190) Nonlinear optics; (190.3270) Kerr effect.

<https://doi.org/10.1364/OPTICA.5.000271>

1. INTRODUCTION

Research in strong-field physics and attosecond science has triggered a need for high-intensity ultrashort laser sources in the mid-infrared [1–3]. Currently, the most common generation and amplification methods are based on second-order nonlinearity, such as chirped pulse optical parametric amplifiers (OPAs) with periodically poled optical phase matching gratings [4–6]. Recently, potential for single-cycle infrared pulse generation by difference frequency generation has been demonstrated [7]. State-of-the-art OPAs supply amplification factors of up to three orders of magnitude with amplified pulses in the energy range of tens of μJ in dependence on seed wavelength, corresponding to 5%–10% of the pump energy.

Although OPAs are currently the leading technology for ultrashort mid-infrared pulse amplification, their development is challenging. For their efficient operation, a series of stringent conditions must be met, which are intimately connected to the properties of second-order nonlinear crystals. Amplification of single-cycle pulses either requires thin crystals (reducing the efficiency) or low dispersion across a spectrum covering the frequencies of the three interacting waves. Moreover, many second-order nonlinear crystals absorb light in the mid-infrared, and moderate damage thresholds also present a limitation.

The process corresponding to OPAs in χ^3 -nonlinear materials is parametric four wave mixing [8,9]. Here we investigate a new mechanism for mid-infrared amplification based on Kerr instability, which we call Kerr instability amplification (KIA). In a Kerr nonlinear material, parametric four-wave mixing processes of the type $\omega_p + \omega_p - (\omega_p \pm \Omega_s) = \omega_p \mp \Omega_s$ occur, during which two photons ω_p of the pump field are converted into fields $\epsilon_x(\Omega_s)$ and

$\epsilon_x^*(-\Omega_s)$ with photon energies shifted, respectively, to the red and blue sides of ω_p by Ω_s (see Fig. 1). Coupling between the red and blue sides of the pulse introduces unstable solutions in addition to conventional four wave mixing. For a wide range of seed frequencies in the interval $-\omega_p < \Omega_s < \omega_p$, there exist transverse wavevectors k_\perp for which exponential growth occurs. As the transverse wavevector for maximum amplification $\bar{k}_\perp(\Omega_s)$ is finite, the emission is noncollinear with the pump pulse. The wavevectors of the instability $\mathbf{K}(\pm\Omega_s)$ fulfill the relation $\mathbf{K}(\Omega_s) = 2\mathbf{K}_p + \mathbf{K}(-\Omega_s)$ (see Fig. 1), so that, in contrast to four wave mixing, phase matching is fulfilled automatically. Outside the unstable range, the phases of $\epsilon_x(\Omega_s)$ and $\epsilon_x^*(-\Omega_s)$ are mismatched and regular four-wave mixing dynamics ensues. We suggest and theoretically demonstrate that through this instability a Kerr nonlinear material irradiated by a high-intensity pump pulse can act as an amplifier for a noncollinear seed pulse.

It is well known that intense laser pulses propagating in Kerr nonlinear materials result in self-focusing, breakup, and formation of stable filaments. From these filaments, conical emission occurs—emission of broadband radiation at a frequency-dependent angle to the filament (for a review, see Ref. [10]). KIA is based on the same unstable process as conical emission, although it occurs long before filamentation, in the limit where the Kerr nonlinearity has not modified the pump pulse substantially. Substantial progress on understanding filamentation [11–14] and modulation instabilities [15–18] has been made over the past 50 years. All of this work relies on an expansion of the seed wavevector in a Taylor series of dispersive and transverse wavevector terms. This works well for gases [14] where only the first few terms contribute. However, KIA in

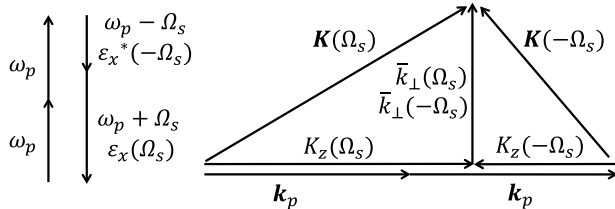


Fig. 1. Schematic of KIA. Left: parametric four-wave mixing of type $2\omega_p - (\omega_p \pm \Omega_s) = \omega_p \mp \Omega_s$, where ω_p is the pump frequency and $-\omega_p < \Omega_s < \omega_p$ is the seed frequency. Right: there exist transverse wavevectors for which unstable behavior occurs. Gain is maximum for the transverse wavevector $\vec{k}_\perp(\Omega_s)$. The instability evolves as $\epsilon_x(\Omega_s) = \exp(i(\omega_p + \Omega_s)t - iK(\Omega_s)x)$ and $\epsilon_x^*(-\Omega_s) = \exp(-i(\omega_p - \Omega_s)t + iK(-\Omega_s)x)$. Here, $K(\Omega_s) = (\vec{k}_\perp(\Omega_s), 0, K_z(\Omega_s))$. In contrast to conventional four wave mixing, phase matching of the instability is automatically fulfilled as the wavevector of the instability $K(\Omega_s)$ fulfills the relation $K(\Omega_s) = 2K_p + K(-\Omega_s)$. For a more detailed discussion, see Eq. (12) and below.

dielectrics can occur over wide spectral ranges and with large transverse wavevectors for which the expansion cannot be cleanly terminated. The resulting summation becomes impractical and convergence is questionable. Therefore, an extended linear stability analysis has been developed to remedy these limitations.

Our theoretical results are used for a feasibility analysis of KIA on the basis of two infrared materials, CaF₂ and KBr. Analytical expressions of the amplified seed pulse profile serve as a tool for designing Kerr instability amplifiers. We find that it is possible to amplify 1–2 cycle pulses with wavelengths from 1 to 14 μm, which exceeds current OPA capacities. Amplification by 3–4 orders of magnitude and energies in the range of a few tens of μJ are comparable to OPAs, whereas the predicted conversion efficiency of 0.25% of pump energy is lower. We believe that with optimization and further progress in the development of infrared pump laser sources, KIA has potential to become a versatile tool for ultrashort pulse amplification in the infrared.

2. THEORY OF KERR INSTABILITY AMPLIFICATION

In what follows, an extended linear stability analysis is developed, which allows modeling Kerr instability emission over its whole spectral and transverse wavevector range. A summary of all the parameters and definitions used in our derivation is given in [Supplement 1](#) [19].

Our analysis of KIA starts from the scalar wave equation for a Kerr [$\chi^{(3)}$] nonlinear material for the electric field $E(x, t) = E_p \hat{x} \exp(i\omega_p t - ik_p z) + \epsilon_x(x, t) + \text{c.c.}$. The electric field is chosen to be a superposition of a pump continuous wave (cw) polarized along x and a perturbation ϵ_x . Here E_p is the pump electric field strength, ω_p is the pump laser frequency, and k_p is the pump wavevector defined below. Coupling to other polarization directions is small, as determined by Gauss's law resulting in $O(\epsilon)$ in $\nabla \epsilon = 0$. Inserting the Ansatz into the scalar wave equation and keeping only terms $O(\epsilon_x)$ gives

$$\left(\partial_z^2 + \nabla_\perp^2 - \frac{\partial_t^2}{c^2} n^2 \star \right) \epsilon_x = \frac{E_p^2 \partial_t^2}{c^2} \chi^{(3)} \star P(\epsilon_x), \quad (1)$$

with $P = 6\epsilon_x + 3\epsilon_x^* \exp[2i(\omega_p t - k_p z)]$. The cw field is a solution of the vector wave equation for k_p =

$(n_p^2 + n_n(\omega_p))^{1/2} \omega_p/c$ and drops out of Eq. (1). Here $n(\omega)$ is the linear refractive index defined in the frequency domain, $n_p = n(\omega_p)$, $n_n = 3\chi^{(3)} E_p^2 = n_2 I_p$ is the nonlinear refractive index with n_2 the optical Kerr nonlinearity coefficient, and I_p is the pump intensity. Frequency dependence of n and n_2 results in a convolution in the time domain, which is represented by the star symbol \star . Although the theory can be developed for frequency-dependent n_n [14], we decided to keep n_2 constant from here on to avoid additional complexity. Estimates below show that this is a reasonable approximation for the examples considered here.

Next, we define $\epsilon_x = v_x(x, t) \exp(i\omega_p t - ik_p z)$ and perform a Fourier transform of Eq. (1) from coordinates x, y, t to $\mathbf{k}_\perp, \Omega = \omega - \omega_p$, where $\mathbf{k}_\perp = (k_x, k_y)$ defines the transverse wavevector. The Fourier transform is denoted as $\hat{F}(\epsilon_x) = \tilde{\epsilon}_x(z, \omega, \mathbf{k}_\perp) = \tilde{v}_x(z, \Omega, \mathbf{k}_\perp) \exp(-ik_p z)$. The Fourier-transformed wave equation is

$$[(\partial_z - ik_p)^2 + k_v^2 - k_\perp^2] \tilde{v}_x = -k_n^2 \tilde{v}_{x(-)}, \quad (2)$$

where $k_v^2(\omega) = k^2(\omega) + 2k_n^2(\omega)$ is the wavevector experienced by the perturbation; it is composed of a linear contribution, $k = \omega c$, and a nonlinear wavevector, $k_n = n_n^{1/2} \omega c$. $k_\perp^2 = k_x^2 + k_y^2$ is the transverse wavevector squared. Further, we use the notation $\tilde{v}_x^*(-\Omega) = \tilde{v}_{x(-)}$. Note that the wavevector k_v of the perturbation contains twice the nonlinearity of the pump wavevector, k_p . Also, we assume a small nonlinearity, $n_n/n^2 \ll 1$. Materials for which $n \rightarrow 0$ violate this assumption and require separate consideration [20].

The equation for $\tilde{v}_{x(-)}$ is obtained by taking the complex conjugate of Eq. (2) and by replacing $\Omega \rightarrow -\Omega$ in all Ω -dependent functions:

$$[(\partial_z + ik_p)^2 + k_{v(-)}^2 - k_\perp^2] \tilde{v}_{x(-)} = -k_n^2 \tilde{v}_x. \quad (3)$$

Here, $k_{v(-)}^2 = k_v^2(\omega_p - \Omega)$, and the minus in $k_{v(-)}^2$ has the same meaning.

In order to make further progress the sign-swapped functions need to be specified. To this end, they need to be split in even/odd parts that are symmetric/anti-symmetric with regard to sign change. We start with $k_v(\omega)$ and introduce $\eta = \sqrt{n^2 + 2n_n} \approx n + n_n/n$ and $\eta_p = \eta(\omega_p)$. The refractive index can be recast into $\eta(\omega) = \eta_p + \Delta\eta(\Omega)$, where $\Delta\eta(\Omega) = \eta_g(\Omega) + \eta_u(\Omega)$ is split into even and odd parts, $\eta_{g,u} = \frac{1}{2}[\Delta\eta(\Omega) \pm \Delta\eta(-\Omega)]$, so that $\eta_g(-\Omega) = \eta_g(\Omega)$ and $\eta_u(-\Omega) = -\eta_u(\Omega)$. With these definitions, we obtain $k_v = k_v(\omega_p) + D_g + D_u$, where

$$D_g(\Omega) = c^{-1}(\eta_g(\Omega)\omega_p + \eta_u(\Omega)\Omega), \quad (4a)$$

$$D_u(\Omega) = c^{-1}((\eta_p + \eta_g(\Omega))\Omega + \eta_u(\Omega)\omega_p). \quad (4b)$$

Using the above definitions, the sign-swapped wavevector is given by $k_{v(-)} = k_v(\omega_p) + D_g - D_u$. The terms D_g and D_u represent, respectively, the exact even and odd dispersion functions of k_v (see [Supplement 1](#) for plots) [19]. They will be used throughout our analysis. They can be connected to the commonly used dispersion expansion as follows: in the absence of nonlinearity, $\eta_{p,g,u} \rightarrow n_{p,g,u}$ and $k_v \rightarrow k$; for $\Omega/\omega_p \ll 1$, $n_u \approx n'_p \Omega$ and $n_g \approx n'_p \Omega^2/2$ so that to lowest order we obtain from Eq. (4) $D_g \approx (\beta_2/2)\Omega^2$ and $D_u \approx \beta_1 \Omega$, with $\beta_1 = [dk/d\omega](\omega_p) = (n_p + n'_p \omega_p)/c$ the group velocity and $\beta_2 = [d^2 k/d\omega^2](\omega_p) = (n'_p \omega_p + 2n'_p)/c$ the group velocity dispersion; prime and double prime denote first and second frequency derivatives, respectively.

Finally, since we treat n_n as constant, the sign swap operation for the nonlinear wavevector is trivial, $k_{n(-)}^2 = n_n(\omega_p - \Omega)^2/c^2$.

Using Eq. (3) to eliminate $\tilde{v}_{x(-)}^*$ in Eq. (2) results in a fourth-order differential equation. Inserting the Ansatz $\tilde{v}_x \propto \exp(iK_v z)$ with $K_v(\Omega)$ a complex wavevector yields the quartic equation

$$\begin{aligned} & [(K_v^2 - D_u^2\sigma^2) + (D_u^2 - k_p^2)(\sigma^2 - 1) + k_\perp^2]^2 \\ & - 4k_p^2(K_v + D_u\sigma)^2 - k_n^2k_{n(-)}^2 = 0 \end{aligned} \quad (5)$$

with $\sigma(\Omega) = (k_v(\omega_p) + D_g)/k_p$. By using $k_v(\omega_p) \approx k_p + k_n^2(\omega_p)/(2k_p)$, we obtain the approximate expression $\sigma^2 - 1 \approx (k_n(\omega_p)/k_p)^2 + 2D_g/k_p$ for later use. The dominant part of the solution is given by the second term, which gives $K_v \approx -D_u\sigma$. As a result, we can approximate in the first term of Eq. (5) $K_v^2 - (D_u\sigma)^2 \approx -2D_u\sigma(K_v + D_u\sigma)$. This amounts to neglecting backward propagating solutions and results in a reduction to a quadratic equation,

$$\begin{aligned} & 4(K_v + \sigma D_u)^2(k_p^2 - (\sigma D_u)^2) - 4(K_v + \sigma D_u) \\ & \times \sigma D_u(k_\perp^2 - k_p^2) - (k_\perp^2 - k_p^2)^2 + (k_n k_{n(-)})^2 = 0. \end{aligned} \quad (6)$$

Here, $\kappa_\perp^2(\Omega) = (k_p^2 - D_u^2)(\sigma^2 - 1)$. Solution of Eq. (6) yields $K_v = K_u(\Omega) + K_g(\Omega)$ with

$$K_u(\mathbf{k}_\perp, \Omega) = -\sigma D_u \left[1 - \frac{1}{2} \frac{\kappa_\perp^2 - k_p^2}{k_p^2 - (\sigma D_u)^2} \right], \quad (7a)$$

$$K_g(\mathbf{k}_\perp, \Omega) = -\frac{1}{2} \frac{k_p \sqrt{(\kappa_\perp^2 - k_p^2)^2 - \delta_\perp^4}}{k_p^2 - (\sigma D_u)^2}. \quad (7b)$$

δ_\perp^2 is defined below. In the appropriate limits [19], Eq. (7b) goes over into the temporal modulation instability [16], and spatial filamentation instability [11]. The solution of the quadratic equation results in an expression with a square root. When the argument of the square root in K_g is negative, exponential growth occurs with intensity gain $g = -2\text{Im}(K_g)$. In the limit of $k_p^2 = (\sigma D_u)^2$, which occurs for $\Omega \approx \pm\omega_p$, the quadratic equation (6) reduces to a linear equation and K becomes real; this has to be treated separately. For each frequency Ω , the gain g is maximum at the transverse wavevector

$$\bar{k}_\perp(\Omega) = \begin{cases} \kappa_\perp & \text{for } \kappa_\perp^2 \geq 0 \\ 0 & \text{for } \kappa_\perp^2 < 0 \end{cases} \quad (8)$$

and is denoted by $\bar{g} = g(k_\perp = \bar{k}_\perp(\Omega), \Omega)$, with

$$\bar{g}(\Omega) = \begin{cases} \frac{k_p \sqrt{\delta_\perp^4 - (\kappa_\perp^2 - k_p^2)^2}}{k_p^2 - (\sigma D_u)^2} & \text{elsewhere} \\ 0 & \text{for } \kappa_\perp^2 < 0, \kappa_\perp^4 > \delta_\perp^4. \end{cases} \quad (9)$$

The relation $g(k_\perp^2 = \bar{k}_\perp^2 \pm \delta_\perp^2) = 0$, determines the k_\perp -half-width $\delta_\perp(\Omega)$ for a given frequency Ω via the relation

$$\delta_\perp^2(\Omega) = \frac{k_n k_{n(-)}}{k_p} \sqrt{k_p^2 - (\sigma D_u)^2}. \quad (10)$$

The relation $k_\perp^2 = \bar{k}_\perp^2 \pm \delta_\perp^2$ defines curves in the $k_\perp - \Omega$ plane at which gain disappears. The curve defined by the expression with the minus sign exists only for $\kappa_\perp^2 \geq \delta_\perp^2$.

We emphasize that the solution of Eqs. (2) and (3) obtained here is practically exact and only neglects backward propagating solutions. A comparison with a numerical solution of Eqs. (2) and (3) gives indistinguishable results (see Supplement 1) [19].

3. KIA IN THE PLANE WAVE LIMIT

In what follows, we will apply the results of our stability analysis to analyze the KIA of seed plane waves.

A. Theory

A seed plane wave

$$\tilde{v}_x(z=0) = (2\pi)^{3/2} E_s \delta(k_x - \bar{k}_{\perp s}) \delta(k_y) \delta(\Omega - \Omega_s) \quad (11)$$

experiences maximum gain according to the above relations; here, $\bar{k}_{\perp s} = \bar{k}_\perp(\Omega_s)$. After material length l , the electric field is determined by the inverse Fourier transform of $\tilde{v}_x(0) \exp(iK_v l)$, which yields

$$e_x(\mathbf{x}, t) = E_s \exp \left(\frac{1}{2} \bar{g}(\Omega_s) l - i\mathbf{K}_s \cdot \mathbf{x} + i\omega_s t \right). \quad (12)$$

Here, $\mathbf{K}_s = \mathbf{K}(\Omega_s) = (\bar{k}_{\perp s}, 0, K_{zs})$ is the seed wavevector, $K_{zs} = K_z(\Omega_s) = k_p + [\sigma D_u](\Omega_s)$, $\mathbf{x} = (x, y, z = l)$, $\omega_s = \omega_p + \Omega_s$, and E_s is the strength of the seed electric field. We find that optimum amplification takes place when the seed propagation axis lies on a cone around the pump wavevector with half-angle

$$\theta_s = \theta(\Omega_s) = \arctan(\bar{k}_{\perp s}/K_{zs}). \quad (13)$$

Note that θ_s is related to but not necessarily the same as the conical emission angle. Conical emission grows out of noise and operates in the regime where filamentation has drastically modified the pump pulse. Seeded amplification occurs over distances long before filamentation sets in.

Further, we would like to point out that KIA is automatically phase-matched, unlike conventional three- or four-wave mixing processes (see also the schematic in Fig. 1). The space-dependent phases of the perturbation terms are $\tilde{v}_x \propto \exp(-i\mathbf{K}(\Omega_s)\mathbf{x})$ and $\tilde{v}_{x(-)}^* \propto \exp(i\mathbf{K}(-\Omega_s)\mathbf{x})$. As $\bar{k}_\perp(\Omega_s) = \bar{k}_\perp(-\Omega_s)$ and $K_z(-\Omega_s) = -K_z(\Omega_s)$, the left- and right-hand sides of Eq. (2) are phase-matched. This is not the case outside the instability regime where K_g becomes real, as $K_g(\Omega_s) = K_g(-\Omega_s)$, which is the conventional regime of four-wave mixing.

B. Discussion of Results

Equations (7)–(13) characterize KIA over the whole frequency and transverse wavevector space. In what follows, these equations are discussed on the basis of CaF₂ and KBr in Figs. 2 and 3, respectively. We chose two different pump wavelengths of $\lambda_p = 0.85$ and $2.1 \mu\text{m}$. The CaF₂ crystal has a transmission window of $0.3\text{--}8 \mu\text{m}$ [21]; $n_2 = 2 \times 10^{-16} \text{ cm}^2/\text{W}$ [22], whereas n is taken from Ref. [23]. The KBr crystal transmits from 0.25 to $25 \mu\text{m}$ [21]; $n_2 = 6 \times 10^{-16} \text{ cm}^2/\text{W}$ [24], whereas n is taken from Ref. [25].

In Fig. 2(a), the intensity gain profile g from Eq. (7b) is plotted versus ω_s/ω_p and k_\perp/k_p . The full white line represents \bar{k}_\perp ; pump wavelength $\lambda_p = 2\pi c/\omega_p = 0.85 \mu\text{m}$; and pump intensity is $I_p = 50 \text{ TW/cm}^2$. Amplification occurs over a wide spectral range of $0.45\text{--}15 \mu\text{m}$. Gain terminates along two curves, which are defined by the relation discussed below Eq. (10).

In Fig. 2(b), maximum gain \bar{g} is shown on the infrared side versus seed frequency ν_s (bottom axis) and seed wavelength λ_s (top axis). The two pump wavelengths $\lambda_p = 0.85$ and $2.1 \mu\text{m}$ correspond, respectively, to the blue full and green dashed curves in Figs. 2(b) and 2(c). Maximum gain reaches a global maximum when the pump and seed frequencies are equal and drops toward longer wavelengths. Further, \bar{g} increases with pump frequency. For $\lambda_p = 0.85 \mu\text{m}$, the gain is still substantial at $\lambda_s = 15 \mu\text{m}$.

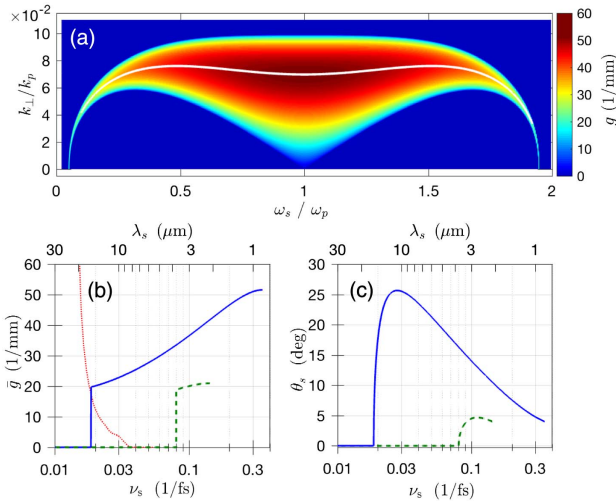


Fig. 2. Plane wave amplification in a CaF_2 crystal with Kerr coefficient $n_2 = 2 \times 10^{-16} \text{ cm}^2/\text{W}$ and pump peak intensity $I_p = 50 \text{ TW}/\text{cm}^2$. (a) Kerr instability gain g versus ω_s / ω_p (seed over pump frequency) and k_{\perp} / k_p (transverse over pump wavevector). Pump wavelength $\lambda_p = 0.85 \mu\text{m}$. The white line indicates \bar{k}_{\perp} at which maximum gain $\bar{g} = g(\bar{k}_{\perp})$ [Eq. (9)] occurs. (b) \bar{g} versus seed frequency ν_s (bottom) and seed wavelength λ_s (top). The red dotted line represents absorption. [(b), (c)] $\lambda_p = 0.85$ and $2.1 \mu\text{m}$ correspond to the blue full and green dashed curves, respectively. (c) Angle of inclination θ_s between pump and seed beam [Eq. (13)] at which maximum amplification takes place versus ν_s and λ_s .

Amplification [$\exp(\bar{g}l)$] by more than four orders of magnitude can be obtained in a crystal of length $l = 0.5 \text{ mm}$. Note that gain and absorption balance each other at $\lambda_s = 20 \mu\text{m}$. As a result, the medium becomes transparent in the presence of the pump beam. For $\lambda_p = 2.1 \mu\text{m}$, the gain extends only over a narrow spectral interval. The reason for this behavior becomes clear from Fig. 2(c) where the angle for maximum amplification, Eq. (13), is plotted for the same two pump wavelengths.

For $\lambda_p = 2.1 \mu\text{m}$, θ_s reaches a maximum close to the pump wavelength and then drops to 0. This property arises from the functional form of $n(\omega)$. The angle θ_s depends on \bar{k}_{\perp} , which depends on $\kappa_{\perp}^2 \propto \sigma^2 - 1 \approx n_n / n_p^2 + (2/n_p)(\eta_g + \eta_u \Omega_s / \omega_p)$ (see Supplement 1 for plots) [19]. Depending on the material and λ_p , the two terms η_g and $\eta_u \Omega_s / \omega_p$ can have opposite or equal signs. In this particular case, they are of opposite signs and comparable magnitudes so that for decreasing ν_s , κ_{\perp}^2 becomes negative. From Eqs. (8) and (9), we see that then $\bar{k}_{\perp} = \bar{g} = 0$ so that both gain and θ_s become 0. Similar behavior can be seen for $\lambda_p = 0.85 \mu\text{m}$, although stretched out over a wider spectral interval.

In Fig. 3, the results for a KBr crystal are shown for a pump intensity of $I_p = 8 \text{ TW}/\text{cm}^2$; same line styles as in Fig. 2 are used. The intensity gain profile g in Fig. 3(a) is plotted for $\lambda_p = 2.1 \mu\text{m}$. In contrast to CaF_2 , in KBr, $\lambda_p = 2.1 \mu\text{m}$ works very well and gain extends up to twice the transmission window [see also Fig. 3(b)]. The maximum gain is still substantial at the edge of the transmission window (see the red dotted line). Amplification of more than four orders of magnitude can be achieved over a crystal length of $l = 2 \text{ mm}$. For $\lambda_p = 0.85 \mu\text{m}$, the gain is confined to a narrower spectral range (up to $8 \mu\text{m}$). The reason for this becomes clear from Fig. 3(c).

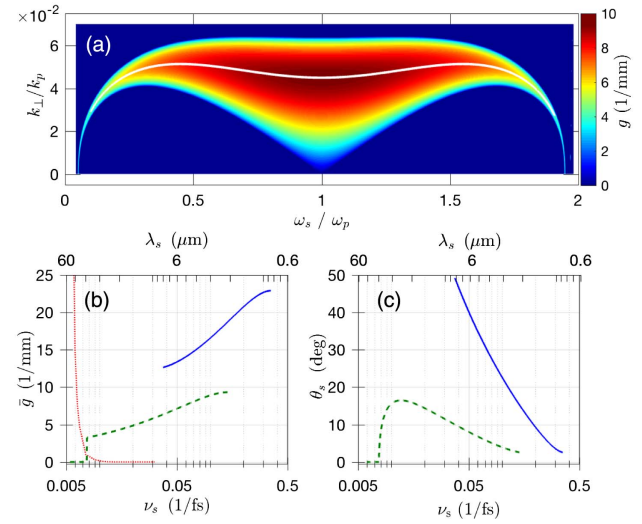


Fig. 3. Plane wave amplification in a KBr crystal. Panels (a)–(c) correspond to those in Fig. 2. Here we have a nonlinear refractive index of $n_2 = 6 \times 10^{-16} \text{ cm}^2/\text{W}$ and a pump peak intensity of $I_p = 8 \text{ TW}/\text{cm}^2$. In panel (a), the pump wavelength is $\lambda_p = 2.1 \mu\text{m}$. All other parameters and definitions in panels (a)–(c) are the same as those in the caption of Fig. 2.

For $\lambda_p = 0.85 \mu\text{m}$, the angle rises sharply for increasing seed wavelength. This stems from the fact that both terms in $\sigma^2 - 1$ carry the same sign. Here, gain terminates when the denominator in Eq. (7b) becomes 0 for $k_p = \sigma D_w$. By contrast, for $\lambda_p = 2.1 \mu\text{m}$, the signs are again different and we see similar behavior as in Fig. 2(c). Clearly, $n(\omega)$ strongly influences KIA and therefore presents a critical design parameter.

The ultrawide frequency band and the large noncollinear angles θ_s encountered in Figs. 2 and 3 underline the necessity of our extended theoretical framework, which does not rely on dispersion expansion and paraxial approximation.

4. KIA OF FINITE PULSES

In extension of our plane wave analysis above, we explore KIA of finite pulses in a noncollinear setup with seed and pump pulses inclined at the optimum gain angle of θ_s .

A. Theory

Our analysis relies on assuming a pump plane wave. This is justified as long as the pump pulse is wider than the seed pulse so that its intensity varies weakly over the seed pulse. The seed pulse is assumed to be inclined at θ_s along x with Gaussian spatial and temporal profiles, and field strength E_s . The spatial and temporal $1/e^2$ -widths are $w_x(0) = w_x = 2/\Delta_x$, $w_y(0) = w_y = 2/\Delta_y$, and $\tau = \tau(0)$, respectively. The initial Gaussian seed pulse in the Fourier domain is given by

$$\tilde{v}_x(0) = \frac{2^{3/2} E_s f(\Omega)}{\Delta_x \Delta_y \Delta_\omega} \exp \left(-\left(\frac{k_x - \bar{k}_{\perp s}}{\Delta_x} \right)^2 - \left(\frac{k_y}{\Delta_y} \right)^2 \right), \quad (14)$$

where $f = \exp(-(\Omega - \Omega_s)^2 / \Delta_\omega^2)$ with $\Delta_\omega(0) = \Delta_\omega = 2/\tau$. As the transverse wavevector of maximum amplification $\bar{k}_{\perp}(\Omega)$ varies as a function of frequency (transverse), the beam center and amplification maximum move increasingly apart with growing $|\Omega - \Omega_s|$. In the strong amplification limit, the transverse beam

center will align with the amplification maximum, resulting in an angular chirp [26], i.e., different frequency components have slightly different transverse wavevector centers. The amplified pulse spectrum can be approximately evaluated analytically by Taylor-expanding the gain g about $\bar{k}_\perp(\Omega)$. To leading order, this results in a Gaussian intensity amplification profile where

$$g \approx \bar{g} - g_2(k_x - \bar{k}_\perp)^2, g_2 = 2k_p\bar{k}_\perp^2[\delta_1^2(k_p^2 - (\sigma D_u)^2)]^{-1}. \quad (15)$$

The gain only modifies the k_x pulse profile. Together with Eq. (7a), we obtain the Fourier beam amplitude after amplifier length l ,

$$\begin{aligned} \tilde{v}_x(\mathbf{k}_\perp, l, \Omega) &= \tilde{v}_x(0) \exp\left(-i\sigma D_u l + \frac{1}{2}\bar{g}l\right) \exp\left(-\frac{i}{2}\alpha l k_y^2\right) \\ &\times \exp\left(-\frac{l}{2}(g_2 + i\alpha)(k_x - \bar{k}_\perp)^2 - i\alpha l \bar{k}_\perp(k_x - \bar{k}_\perp)\right), \end{aligned} \quad (16)$$

where $\alpha(\Omega) = \sigma D_u / (k_p^2 - (\sigma D_u)^2)$. Propagation in free space after the amplifier is not considered here.

Inverse Fourier transform with regard to \mathbf{k}_\perp gives a complex shifted Gaussian beam

$$\begin{aligned} \tilde{v}_x(x, y, l, \Omega) &= \frac{E_s \tau w_x w_y}{\sqrt{2q_x q_y}} f(\Omega) \exp\left(\left(\frac{\gamma}{2} - ix\right)l + ik_\perp s x\right) \\ &\times \exp\left(-\frac{(x - x_c)^2}{q_x} - \frac{y^2}{q_y}\right) \end{aligned} \quad (17)$$

with $\gamma = \bar{g} - g_2(\bar{k}_\perp - \bar{k}_{\perp s})^2$ and $x = \sigma D_u - (\alpha/2)(\bar{k}_\perp^2 - \bar{k}_{\perp s}^2)$. Further, $q_x = w_x^2 + 2(g_2 + i\alpha)l$ and $q_y = w_y^2 + 2i\alpha l$ are related to the $1/e^2$ -beam widths via $w_{x,y}^2(l) = |q_{xy}|^2 / \text{Re}(q_{x,y})$, and the complex shift of beam center is given by $x_c = x_{cr} + ix_{ci} = \alpha l \bar{k}_{\perp s} + ig_2 l (\bar{k}_\perp - \bar{k}_{\perp s})$. We use the following notation: subscript, s , denotes (Ω_s) ; otherwise, the argument is (Ω) .

From Eq. (17), the intensity spectrum follows as

$$\begin{aligned} |\tilde{v}_x(x, y, l, \Omega)|^2 &= \frac{(E_s \tau w_x w_y)^2}{2|q_x q_y|} |f(\Omega)|^2 \exp(\Gamma l) \\ &\times \exp\left(-\frac{2(x - \xi_{cr})^2}{w_x^2(l)} - \frac{2y^2}{w_y^2(l)}\right). \end{aligned} \quad (18)$$

Due to contributions from the imaginary parts in the exponent of Eq. (17), the shift of the beam center changes to $\xi_{cr} = x_{cr} + x_{ci}(\text{Im}(q_x)/\text{Re}(q_x))$; the gain changes to $\Gamma = \bar{g} - g_2(\bar{k}_\perp - \bar{k}_{\perp s})^2(w_x^2/\text{Re}(q_x))$. Taylor expansion of the gain about Ω_s yields $\Gamma(\Omega) = \Gamma_s + \Gamma'_s(\Omega - \Omega_s) + (1/2)\Gamma''_s(\Omega - \Omega_s)^2$. As a result, the amplified spectrum remains Gaussian. Integration over Ω by using the method of stationary phase results in a spectral $1/e^2$ -width $\Delta_\omega(l) = 2/\tau_g(l)$. Here, $\tau_g(l) = (\tau^2 - \Gamma''_s l)^{1/2}$ is the gain-modified, transform-limited temporal $1/e^2$ -duration, which corresponds to the actual pulse duration $\tau(l)$ when the spectral chirp is neglected. Integration over transverse coordinates yields the amplified seed pulse energy

$$\frac{W_s(l)}{W_s(0)} = \frac{w_x}{\sqrt{\text{Re}[q_x(\Omega_s)]}} \frac{\tau}{\tau_g(l)} \exp\left(\Gamma_s l + \frac{(\Gamma'_s l)^2}{2\tau_g^2(l)}\right), \quad (19)$$

where $W_s(0) = (\pi/2)^{3/2} I_s \tau w_x w_y$ and I_s are, respectively, the initial seed pulse energy and intensity. Finally, spatiotemporal profiles and $\tau(l)$ are determined numerically from Eq. (17).

B. Results

KIA operates in the limit where the amplified seed intensity is small compared with the pump peak intensity, so that the nonlinear terms in Eq. (1) are negligible. This is fulfilled for $I_s(l) = I_p/10$ [27]. The corresponding amplified seed pulse energy is $W_s(l) = (\pi/2)^{3/2} I_s(l) \tau(l) w_x(l) w_y(l)$, from which, together with Eq. (19), the initial pulse energy and intensity are obtained. For KIA in CaF₂ and KBr, a material length of $l = 8/\bar{g}(\omega_s)$ is assumed corresponding to a plane wave amplification factor of $\exp(8) \approx 3000$. l is changed with ω_s to make the plane wave amplification factor constant for all frequencies.

Efficient amplification requires the seed pulse to stay close to the pump pulse center over l . This requirement sets a lower limit for the pump pulse duration and width, and thus for the minimum pump energy.

There are four factors that cause an increase in pump energy requirements: (i) the inclination between the pump and seed pulse axes, resulting in a walk-off of ξ_{cr} between beam centers; (ii) widening of the seed beam widths, $w_{x,y}(l)$, due to diffraction and transverse spectral gain narrowing; (iii) a temporal walk-off, $\Delta\beta_1 l$, caused by the difference $\Delta\beta_1 = \beta_{1s} - \beta_1$ between seed group velocity $\beta_{1s} = [dK_u/d\Omega](\Omega_s)$ and pump group velocity β_1 defined below Eq. (4); and (iv) lengthening of the seed pulse duration $\tau(l)$ due to spectral gain narrowing and dispersive effects.

The four conditions above determine the required pump pulse parameters as $w_p = r(w_x(l) + 0.5|\xi_{cr}|)$ and $\tau_p = r(\tau(l) + 0.5|\Delta\beta_1|l)$. The factor 1/2 comes from the assumption that the pump and seed beam centers are aligned at half of the material length. We chose the factor by which the pump beam is wider than the final shifted seed beam as $r = 3$ [27]. As a result, the minimum pump energy for KIA to operate efficiently is $W_p = (\pi/2)^{3/2} I_p \tau_p w_p^2$ assuming a radially symmetric transverse pump beam.

A number of other processes that can potentially limit KIA need to be considered. Self-focusing needs to be controlled. Critical self-focusing can be avoided by making the pump beam radius wide enough. We determine w_p from the requirement that the material length $l = l_{sf}/5$, where $l_{sf} = w_p(n_p/(2n_n))^{1/2}$ is the distance for critical self-focusing [28]. The initial seed beam width w_x is determined from a solution of

$$l_{sf} \sqrt{\frac{2n_n}{n_p}} = w_p = r(w_x(l) + 0.5|\xi_{cr}|) \quad (20)$$

with $w_x(l)$ defined below Eq. (17). We assume $w_y = w_x$.

Small-scale self-focusing is a consequence of the Kerr instability; it amplifies the noise superimposed onto the pump beam, which ultimately results in filamentation [13]. The breakup develops at $\bar{k}_\perp(\omega_p)$ where the gain is maximum. By using $\bar{g}(\omega_p)l = 8$, we obtain the gain for the pump noise, $\bar{g}(\omega_p)l = 8\bar{g}(\omega_p)/\bar{g}(\omega_s)$. For example, for $\omega_s/\omega_p = 0.2$, we find from Figs. 3 and 4 that $\bar{g}(\omega_p)/\bar{g}(\omega_s) \approx 1.5$. As a result, the ratio of peak pump signal and noise has to be $> e^{12} \approx 10^5$ to avoid pump beam breakup during KIA. In the examples discussed below, the transverse momentum width of the pump is by an order of magnitude smaller than $\bar{k}_\perp(\omega_p)$ so that potential pump noise can be cleaned with a pinhole before KIA.

Pump pulse lengthening is a consequence of interplay between nonlinear phase modulation and group velocity dispersion.

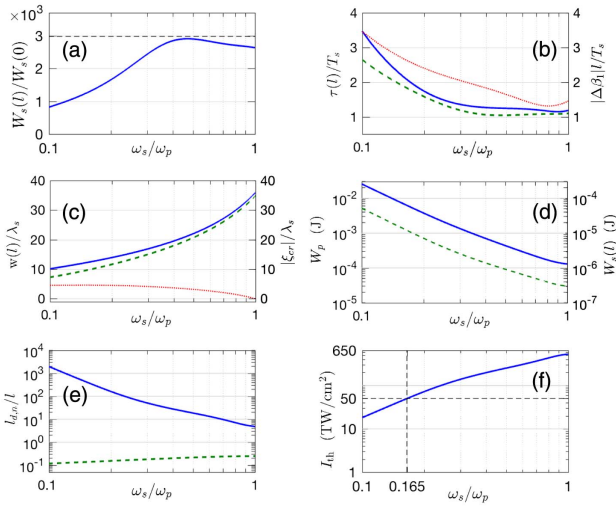


Fig. 4. KIA of a single-cycle pulse $\tau(0) = T_s = 2\pi/\omega_s$ in CaF_2 . Here $n_2 = 2 \times 10^{-16} \text{ cm}^2/\text{W}$, pump peak intensity $I_p = 50 \text{ TW}/\text{cm}^2$, pump wavelength $\lambda_p = 0.85 \mu\text{m}$, and amplifier length $l = 8/\bar{g}$. Pump beam radius and duration are denoted with, respectively, w_p and τ_p [see text above Eq. (20)]. Initial seed beam radii, $w_x(0) = w_y(0)$, are determined from Eq. (20). (a) Seed pulse energy increase, $W_s(l)/W_s(0)$, from Eq. (19) versus ω_s/ω_p (seed over pump frequency). The black dashed line corresponds to the cw limit $\exp(\bar{g}l) = \exp(8) \approx 3000$. (b) Amplified seed pulse duration $\tau(l)/T_s$ (blue, full); transform-limited amplified seed pulse duration $\tau_g(l)/T_s$ [defined above Eq. (19)] (green, dashed); and group velocity walk-off between pump and seed, $|\Delta\beta_1|l/T_s$, versus ω_s/ω_p (red, dotted). (c) Amplified seed beam radii $w_x(l)/\lambda_s$ (blue, full) and $w_y(l)/\lambda_s$ (green, dashed) versus ω_s/ω_p . Initial beam radius is not plotted as $w_y(l) \approx w_x(0) = w_y(0)$. Shift of seed beam center, $|\xi_{cr}|$, is defined below Eq. (18) (red dotted). (d) Minimum required pump energy W_p (blue, full) [see text above Eq. (20)] and corresponding seed energy $W_s(l)$ (green, dashed) versus ω_s/ω_p . (e) Dispersive length l_d/l (blue, full) and nonlinear length l_n/l (green, dashed) versus ω_s/ω_p . (f) Damage threshold intensity I_{th} versus ω_s/ω_p . The dashed lines indicate $I_p = I_{\text{th}}$.

Its influence is measured through the nonlinear length $l_n = 2k_p/k_n^2 = 2n_p c/(n_n \omega_p)$ and dispersive length $l_d = 2\tau_p^2/\beta_2$ of the pump pulse. In the limit of strong KIA, the nonlinear length is shorter than the material length. As a result, $l_d \gg l$ to avoid pump pulse stretching through the combined action of nonlinear phase modulation and dispersion.

Material damage and ionization limit the pump peak intensity to the material damage threshold intensity $I_{\text{th}} = (2/\pi)^{1/2} F_{\text{th}}/\tau_p$. We use damage threshold fluence values F_{th} from the literature. Ionization becomes important around the damage intensity, which results in pump pulse absorption and defocusing through the free-electron lens [10] (for a more detailed discussion, see Supplement 1) [19]. Recently, KIA factors >1000 have been demonstrated in YAG with $\tau_p = 140 \text{ fs}$ and $I_p = 8 \text{ TW}/\text{cm}^2$, which is comparable to the parameters used below [27]. The damage fluence for YAG is $F_{\text{th}} \approx 1.4 \text{ J}/\text{cm}^2$. Ionization did not present a limiting factor, not even at intensities close to the damage threshold.

Contributions from the frequency dependence of the Kerr nonlinearity are small. In the wavelength range of interest here, far away from the bandgap, the electronic part of n_2 undergoes

little variation [29]. The Raman response times of $\approx 0.5\text{--}1 \text{ ps}$ are longer than the seed and pump pulse durations used in the analysis below, which justifies neglecting the frequency dependence [30,31].

The quantitative results for finite-pulse KIA in CaF_2 and KBr for a material length of $l = 8/\bar{g}(\Omega_s)$ are shown in Figs. 4 and 5, respectively. The pump peak intensities for CaF_2 and KBr are chosen as $I_p = 50 \text{ TW}/\text{cm}^2$ and $I_p = 8 \text{ TW}/\text{cm}^2$, respectively. Following the results of the plane wave analysis above, we chose $\lambda_p = 0.85 \mu\text{m}$ and $\lambda_p = 2.1 \mu\text{m}$ for CaF_2 and KBr, respectively. The damage threshold fluences of CaF_2 and KBr in the sub-picosecond pulse duration regime are $F_{\text{th}} = 6.7 \text{ J}/\text{cm}^2$ and $F_{\text{th}} = 3.3 \text{ J}/\text{cm}^2$ [32], respectively (for n_2 see caption). We assume single-cycle initial seed pulses with $I_s(l) = I_p/10$. The initial seed pulse radius is determined from a solution of Eq. (20).

The increase in seed pulse energy, $W_s(l)/W_s(0)$, in Fig. 4(a) is close to the plane wave value of $\exp(\bar{g}l) \approx 3000$ (black, dashed line) for $\omega_s/\omega_p \geq 0.5$ and drops from there. At $\omega_s/\omega_p = 0.2$, amplification is still more than a factor of 1000.

In Fig. 4(b), the $1/e^2$ -pulse duration $\tau(l)$ (blue, full) is obtained from a transverse space integration over the spatiotemporal intensity profile. The intensity profile is calculated as the absolute square of the Fourier transform of Eq. (17). The pulse duration $\tau(l)$ is compared to $\tau_g(l)$ (green, dashed), which is the corresponding transform-limited (chirp-free) pulse duration defined below Eq. (18). The comparison shows that amplification of up to $\omega_s/\omega_p \approx 0.3$ of single-cycle pulses is possible and that the influence of dispersive effects is weak. Even at $\omega_s/\omega_p = 0.2$, amplification of two-cycle pulses is still feasible. Below that the pulse duration rises quickly due to a mixture of gain and dispersive widening. The spectral chirp incurred during KIA is dominantly linear (see Supplement 1) [19] and can be compensated in a post-compression stage. The resulting pulses are transform-limited pulses with duration $\tau_g(l)$. Finally, the red dotted line indicates the shift between peak of seed and pump pulse due to group velocity mismatch.

Widening of the seed beam radius is not dramatic, as can be seen in Fig. 4(c). This is due to the fact that a large pump beam

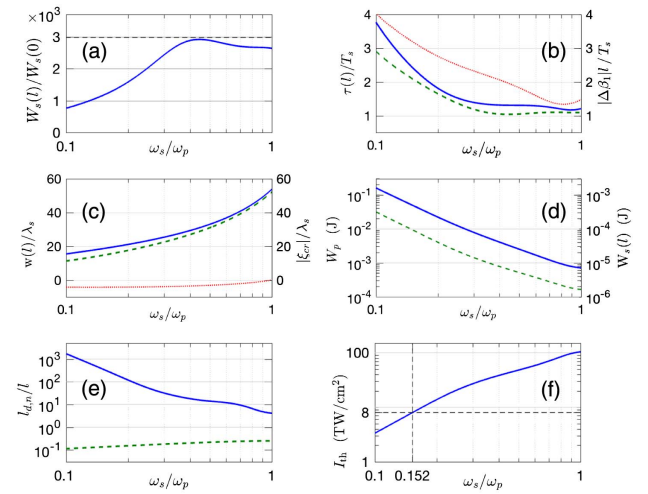


Fig. 5. KIA of a single-cycle pulse $\tau(0) = T_s$ in KBr. Here $n_2 = 6 \times 10^{-16} \text{ cm}^2/\text{W}$, pump peak intensity is $I_p = 8 \text{ TW}/\text{cm}^2$, and pump wavelength is $\lambda_p = 2.1 \mu\text{m}$. Panels (a)–(f) correspond to those in Fig. 4 (see the caption of Fig. 4 for a complete description).

radius is required to avoid self-focusing. This results in a large seed beam radius, as in our above design considerations, the seed radius increases proportionally with the pump radius. In general, it is desirable to choose the seed beam radius to be as large as possible to optimize energy extraction from the pump beam. We find that (green, dashed) $w_y(l) \approx w_x(0) = w_y(0)$, which is why the initial pulse radii are not plotted. Amplification moderately widens $w_x(l)$ (blue, full), as defined below Eq. (17), and results in a beam asymmetry, which is weak over most of the frequency range.

In Fig. 4(d), the minimum pump pulse energy needed for KIA to work and the corresponding amplified seed pulse energy are plotted versus ω_s/ω_p . Naturally, higher seed energies can be obtained when more pump energy is available. At $\omega_s/\omega_p = 0.2$, we find that $W_p = 4$ mJ, which is comfortably available in Ti:sapphire laser systems. The pump energy is larger than the final seed energy by a factor of about 400–500.

The nonlinear length l_n (green, dashed) is shorter than the amplifier length [see Fig. 4(e)]. The dispersive length l_d (blue, full) is between 2 and 4 orders of magnitude longer than the medium length so that no significant pump pulse distortions are expected through the interplay of Kerr nonlinearity and group velocity dispersion.

Finally, Fig. 4(f) shows the damage threshold intensity, I_{th} , for a pump pulse with pulse duration $\tau(l)$. The dashed line indicates the value of $\omega_s/\omega_p = 0.165$ at which $I_p = I_{\text{th}}$. As a result, we can conclude that amplification for a wavelength range between $\lambda_s = 0.85$ μm and $\lambda_s \approx 5.2$ μm is possible. The damage intensity presents a main limitation in extending KIA to even longer wavelengths. Note that toward higher ω_s , damage does not present a problem. I_{th} increases quickly due to shorter required pump pulse durations.

The results for KBr in Fig. 5 are qualitatively similar to what was found for CaF₂ in Fig. 4; therefore, we focus on a discussion of Figs. 5(d) and 5(f). The minimum required pump energy is $W_p \approx 20$ mJ at $\omega_s/\omega_p = 0.2$. This is in the range of what can be achieved by current state-of-the-art Ho:YAG femtosecond amplifier systems operating at wavelengths of $\lambda_p = 1.9$ –2.1 μm [4]. The corresponding seed amplified energy is $W_s \approx 50$ μJ. From Fig. 5(f), we find that KIA is possible to $\lambda_s \approx 14$ μm. For single-cycle KIA, a high I_p is necessary to minimize pulse widening. For KIA operation at lower I_p , see Ref. [19].

Finally, it is interesting to look at the quality of the amplified pulses. Again our two systems behave fairly similar, which is why we show only the results for CaF₂ and $\lambda_p = 0.85$ μm. For other parameters, see Fig. 4. In Figs. 6(a) and 6(c), the spatio-spectral intensity profile, $|\tilde{e}_x(x, y = 0, z = l, \omega)|^2$, is plotted for $\omega_s/\omega_p = 0.2$ and 0.4, respectively. Figures 6(b) and 6(d) show the corresponding spatiotemporal profiles, $|e_x(x, y = 0, z = l, t)|^2$. The peak values are normalized to unity. The spectrum peak is shifted off $\omega/\omega_s = 1$ toward higher frequencies. This stems from the fact that the blue part of the seed spectrum is amplified more strongly, as the maximum gain \bar{g} in the range $\omega_s/\omega_p \leq 0.4$ increases toward higher seed frequencies. Further, the spectrum exhibits some asymmetry, which is not contained in the quadratic expansion of Γ below Eq. (18). Accounting for it analytically would require expansion to third order. The fact that maximum gain \bar{g} is experienced at the finite transverse wavevector $\vec{k}_\perp(\Omega)$, the value of which is frequency-dependent, results in a Gaussian pulse in space domain shifted by x_c [see Eq. (17)]. The real part of the shift, ξ_{cr} , manifests as an off-axis shift of the pulse center [see white line in

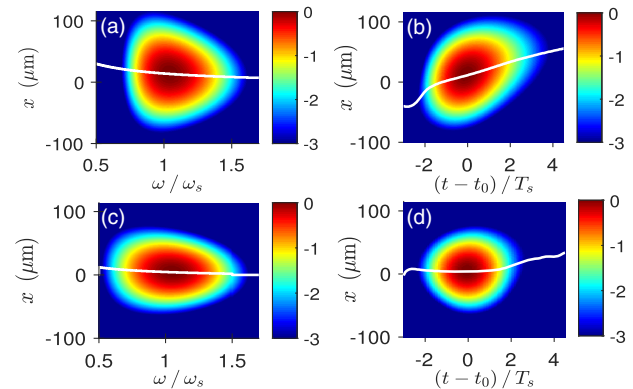


Fig. 6. [(a), (c)] Spatio-spectral and [(b), (d)] spatiotemporal intensity profiles of seed pulses amplified in CaF₂ for $\omega_s/\omega_p = 0.2$ and 0.4, respectively. The parameters are the same as in Fig. 4. Peaks are normalized to unity. Time is shown with reference to time t_0 of the pulse peak and is normalized to the optical cycle T_s . The white lines indicate the transverse pulse maximum.

Figs. 6(a) and 6(c)]. The shift changes slightly with frequency as a result of angular chirp, i.e., each frequency experiences optimum amplification at a slightly different angle. The angular chirp needs to be compensated for, as otherwise the frequency-dependent shift of the pulse center will continue growing during free-space propagation [27], resulting in a degradation of pulse quality. From the slopes in Figs. 3(b) and 4(b), it can be estimated that $d\theta_s/d\lambda_s = 0.1$ and 0.025 rad/μm for CaF₂ and KBr, respectively. The imaginary part x_{ci} has an effect on the spatiotemporal pulse in Figs. 6(b) and 6(d). It creates an x -dependent group velocity component, which skews the pulse in the x – t plane. The pulse distortion becomes pronounced for $\omega_s/\omega_p \leq 0.2$ and is negligible for $\omega_s/\omega_p \geq 0.35$.

5. CONCLUSION

We have investigated a new mechanism for amplification of mid-infrared pulses based on Kerr instability. Our proof-of-principle theoretical analysis of KIA in CaF₂ and KBr crystals demonstrates the potential to amplify pulses in the wavelength range of ≈ 1 –14 μm. Whereas plane wave amplification in KBr extends up to 40 μm, material damage limits finite-pulse KIA to about 14 μm. There, seed pulse output energies in the range of 50 μJ appear feasible with a ratio of pump to seed pulse energy in the range of 400–500. Our numbers are comparable to the performance of OPAs.

The biggest three advantages of KIA are the capacity of single-cycle pulse amplification, which it is intrinsically phase-matched, and simplicity and versatility. Kerr materials are more easily available than infrared materials with second-order nonlinearity. Further, amplifier wavelength can be selected by simply changing the angle between the pump and seed beams. The biggest drawback is an angular chirp acquired during amplification, which needs to be controlled. There exist methods to that end, from a simple prism to more sophisticated techniques [33].

The results shown here are promising, but most likely still far from optimum. There is a huge parameter space to be explored, such as all potential infrared crystals. Further, KIA can be optimized by determining favorable optical properties (e.g., refractive index) from our theory and then designing corresponding (meta)

materials. Finally, the KIA profile is of Bessel–Gaussian nature. Therefore, KIA should lend itself naturally to the amplification of Bessel–Gauss beams.

Funding. Natural Sciences and Engineering Research Council of Canada (NSERC); Canada Research Chairs.

Acknowledgment. The authors acknowledge discussions with T. J. Hammond.

See [Supplement 1](#) for supporting content.

REFERENCES

1. S. Ghimire, A. D. Dichiara, E. Sistrunk, P. Agostini, L. F. Dimauro, and D. A. Reis, "Observation of high-order harmonic generation in a bulk crystal," *Nat. Phys.* **7**, 138–141 (2011).
2. M. Schultze, E. Bothschafter, A. Sommer, S. Holzner, W. Schweinberger, M. Fiess, M. Hofstetter, R. Kienberger, V. Apalkov, V. S. Yakovlev, M. I. Stockman, and F. Krausz, "Controlling dielectrics with the electric field of light," *Nature* **493**, 75–78 (2013).
3. R. Gattass and E. Mazur, "Femtosecond laser micromachining in transparent materials," *Nat. Photonics* **2**, 219–225 (2008).
4. P. Malevich, G. Andriukaitis, T. Flöry, A. J. Verhoef, A. Fernández, S. Ališauskas, A. Pugžlys, A. Baltuška, L. H. Tan, C. F. Chua, and P. B. Phua, "High energy and average power femtosecond laser for driving mid-infrared optical parametric amplifiers," *Opt. Lett.* **38**, 2746–2749 (2013).
5. B. E. Schmidt, N. Thiré, M. Boivin, A. Laramée, F. Poitras, G. Lebrun, T. Ozaki, H. Ibrahim, and F. Légaré, "Frequency domain optical parametric amplification," *Nat. Commun.* **5**, 3643 (2014).
6. C. Manzoni and G. Cerullo, "Design criteria for ultrafast optical parametric amplifiers," *J. Opt.* **18**, 103501 (2016).
7. P. Krogen, H. Suchowski, H. Liang, N. Flemens, K. Hong, F. X. Kärtner, and J. Moses, "Generation and multi-octave shaping of mid-infrared intense single-cycle pulses," *Nat. Photonics* **11**, 222–226 (2017).
8. E. Rubino, J. Darginavičius, D. Faccio, P. Di Trapani, A. Piskarskas, and A. Dubietis, "Generation of broadly tunable sub-30-fs infrared pulses by four-wave optical parametric amplification," *Opt. Lett.* **36**, 382–384 (2011).
9. M. I. M. Abdul Khudus, F. De Lucia, C. Corbari, T. Lee, P. Horak, P. Sazio, and G. Brambilla, "Phase matched parametric amplification via four-wave mixing in optical microfibers," *Opt. Lett.* **41**, 761–764 (2016).
10. A. Couairon and A. Mysyrowicz, "Femtosecond filamentation in transparent media," *Phys. Rep.* **441**, 47–189 (2007).
11. V. I. Bespalov and V. I. Talanov, "Filamentary structure of light beams in nonlinear liquids," *J. Exp. Theor. Phys. Lett.* **3**, 307–309 (1966).
12. L. W. Liou, X. D. Cao, C. J. McKinstry, and G. P. Agrawal, "Spatiotemporal instabilities in dispersive nonlinear media," *Phys. Rev. A* **46**, 4202–4208 (1992).
13. A. J. Campillo, "Small-scale self focusing," in *Self Focusing: Past and Present*, R. W. Boyd, ed. (Springer, 2009).
14. P. Béjot, B. Kibler, E. Hertz, B. Lavorel, and O. Faucher, "General approach to spatiotemporal modulational instability processes," *Phys. Rev. A* **83**, 013830 (2011).
15. L. A. Ostrovskii, "Propagation of wavepackets and space-time self-focusing in a nonlinear medium," *Sov. Phys. J. Exp. Theor. Phys.* **24**, 797–800 (1967).
16. G. Agrawal, *Nonlinear Fiber Optics*, 5th ed. (Academic, 2012).
17. S. Wen and D. Fan, "Spatiotemporal instabilities in nonlinear Kerr media in the presence of arbitrary higher-order dispersions," *J. Opt. Soc. Am. B* **19**, 1653–1660 (2002).
18. F. Min, X. Yun, W. Quing, and S. Jie-Long, "Modulation instability of non-paraxial beams for self-focusing Kerr media," *J. Shanghai Univ.* **8**, 159–163 (2004).
19. <https://doi.org/10.6084/m9.figshare.5878747>.
20. M. Z. Alam, I. De Leon, and R. W. Boyd, "Large optical nonlinearity of indium tin oxide in its epsilon-near-zero region," *Science* **352**, 795–797 (2016).
21. E. D. Palik, *Handbook of Optical Constants of Solids II* (Academic, 1991).
22. D. Milam, M. J. Weber, and A. J. Glass, "Nonlinear refractive index of fluoride crystals," *Appl. Phys. Lett.* **31**, 822–825 (1977).
23. I. H. Malitson, "A redetermination of some optical properties of calcium fluoride," *Appl. Opt.* **2**, 1103–1107 (1963).
24. R. DeSalvo, A. A. Said, D. J. Hagan, A. W. Van Stryland, and M. Sheik Bahae, "Infrared to ultraviolet measurement of two-photon absorption and n_2 in wide bandgap solids," *IEEE J. Quantum Electron.* **32**, 1324–1333 (1996).
25. H. H. Li, "Refractive index of alkali halides and its wavelength and temperature derivatives," *J. Phys. Chem. Ref. Data* **5**, 329–528 (1976).
26. X. Gu, S. Akturk, and R. Trebino, "Spatial chirp in ultrafast optics," *Opt. Commun.* **242**, 599–604 (2004).
27. G. Vampa, T. J. Hammond, M. Nesrallah, A. Yu Naumov, P. B. Corkum, and T. Brabec, "Light amplification by seeded Kerr instability," *Science* **359**, 673–675 (2018).
28. R. W. Boyd, *Nonlinear Optics*, 3rd ed. (Academic, 2008).
29. M. Sheik-Bahae, D. C. Hutchings, D. J. Hagan, and E. W. Van Stryland, "Dispersion of bound electronic nonlinear refraction in solids," *IEEE J. Quantum Electron.* **27**, 1296–1309 (1991).
30. A. R. Gee, D. C. O'shea, and H. Z. Cummins, "Raman scattering and fluorescence in calcium fluoride," *Solid State Commun.* **4**, 43–46 (1966).
31. J. P. Hurrell, S. P. S. Porto, T. C. Damen, and S. Mascarenhas, "Raman scattering from mixed KBr, KCl crystals," *Phys. Lett. A* **26**, 194–195 (1968).
32. L. Gallais and M. Commandré, "Laser-induced damage thresholds of bulk and coating optical materials at 1030 nm, 500 fs," *Appl. Opt.* **53**, A186–A196 (2014).
33. O. Mendoza-Yero, G. Minguez-Vega, J. Lanzis, and V. Climent, "Diffractive pulse shaper for arbitrary waveform generation," *Opt. Lett.* **35**, 535–537 (2010).